Earthquake rupture through a step-over fault system: A case study of the Leech River Fault, southern Vancouver Island

Ge Li[1] **and Yajing Liu**[1]

[1]Department of Earth and Planetary Sciences, McGill University, Montreal, Québec, H3A 0E8, Canada

Key Points:

- In a step-over fault system, earthquake jumping scenarios depend on factors such as fault geometry and initial stress level.
- The influence of such parameters can be collectively represented by the Over Stress Zone size.
- The possibility of multi-fault rupture should be considered to assess the seismic hazard of the Leech River step-over fault system.

Corresponding author: Ge Li, `ge.li2@mail.mcgill.ca`

Abstract

The Leech River fault (LRF) zone located on the southern Vancouver Island can be interpreted as an extensional step-over system based on geological mapping and microseismicity relocation. It consists of two sub-parallel right-lateral active fault structures: the primary NNE dipping LRF structure to the north, and a secondary sub-vertical structure to the south, possibly an extension of the Southern Whidbey Island fault (SWIF). The possibility of an earthquake rupture nucleated on the LRF jumping across the step-over and continuing propagation on the SWIF has significant implications for seismic hazard of the populated southern Vancouver area. To study earthquake rupture jumping scenarios across the LRF system, we develop a finite-element model to simulate dynamic ruptures governed by a linear slip-weakening frictional law. The stress perturbations radiated from the LRF rupture will induce an Over Stressed Zone (OSZ, where shear stress exceeds static frictional strength) on the SWIF. With the increase of the OSZ size R_e, rupture develops from stopping on LRF (no jumping), to breaking part of the SWIF (self-arresting) or the entire SWIF (break-away). We demonstrate that rupture jumping scenario is a collective result depending on a range of parameters. Target parameters in our study include fault initial stress level, step-over offset distance and fault burial depth. We find that R_e and the receiver fault stress status are the keystone variables directly controlling rupture jumping scenarios, while other parameters exert their influence by resulting in different R_e.

1 Introduction

Fault geometrical complexities can have significant influence on earthquake ruptures. Two types of such geometrical complexities have been well documented by geological surveys and manifested in earthquake ruptures. One type is a main fault intersecting with a secondary, branch fault. For example, the 2002 M_w 7.9 Denali, Alaska, earthquake ruptured ∼220 km along the Denali fault before branching to and continuing on the Totschuda fault for another ∼75 km (Eberhart-Phillips et al., 2003; Bhat et al., 2004; Dunham & Archuleta, 2004). The second type is a fault step-over consisting of two or more fault segments without clear surface signature of linkage. In a fault step-over, under certain conditions, rupture nucleated on one fault (the source fault) is nonetheless capable of jumping across the discontinuity and propagating onto the other fault (the receiver fault). This scenario may result in a longer rupture length and larger earthquake moment or magnitude. Many large continental earthquakes tend to involve rupture propagating across multiple fault segments. For example, the 2016 M_w 7.8 Kaikoura (New Zealand) earthquake ruptured at least 12 individual fault segments (including stepovers of 15 - 20 km), with diverse faulting types and slip orientations, resulting in a total on land rupture length of at least 170 km (Hamling et al., 2017; Cesca et al., 2017; Duputel & Rivera, 2017). Another prominent example of multi-fault earthquake rupture is the 2019 Ridgecrest earthquake sequence with a M_w 7.1 right-lateral mainshock triggered by a M_w 6.4 left-lateral foreshock (Liu et al., 2019). The primary structure ruptured during the mainshock extends in the NE-SW direction and straddles the foreshock slip, forming an L-shaped geometry (Barnhart et al., 2019; Liu et al., 2019) consisting of at least 20 faults (Ross et al., 2019).

The Kaikoura earthquake and the Ridgecrest earthquake highlight the limitations of current seismic hazard models. First, Wesnousky (2006) examined the surficial ruptures of 22 historical earthquakes and showed a rupture will be terminated over an offset distance of 5 km or larger. This threshold has been incorporated in the most well-developed earthquake rupture forecast model in California, the Uniform California Earthquake Rupture Forecast 3 (UCERF3) model (Field et al., 2014), where the possibility of rupture jumping across faults segments separated by a distance >5 km is not considered. According to this model, the Kaikoura earthquake, given the 10 - 15 km jumping distances in some step-overs, would not be considered as a plausible scenario (Hamling et al., 2017). Moreover, both earthquakes ruptured many previously unmapped faults, necessitating the compilation of a more thorough fault database for seismic hazards assessment. Such observations also emphasize the need to update existing seismic hazard assessment studies which ignore the possibility of multiple-fault rupture in a known fault system (Ross et al., 2019).

This need should be specifically recognized for the assessment of seismic hazards posed by the Leech River fault (LRF), the major source of seismic hazard to the densely populated areas in SW British Columbia (Zaleski, 2014; Morell et al., 2017; Kukovica et al., 2019) (Figure 1). While the LRF is not yet included in the current seismic hazard model used in the 2015 National Building Code of Canada (NBCC), its significance as a major seismic hazard source has been recongnized by several recent studies. Based on Lidar detection and ranging investigations, Morell et al. (2017) identified subparallel, steeply dipping topographic features, and quaternary colluvium offset by a total of

$\sim$6 m, which collectively suggest at least two M > 6 earthquakes have occurred along the LRF since approximately 15,000 years ago. With Lidar observation and paleoseismic trenching studies, Morell et al. (2018) further updated the proposition of its seismic activity to demonstrate that at least three earthquakes (M > 6) occurred along this fault within the last 9,000 years. Based on a probabilistic seismic hazard analysis, Kukovica et al. (2019) suggests that, at a 2% probability of exceedance in 50 years, the peak horizontal ground acceleration for the city of Victoria will be increased by 9% to 0.63g from the current value of 0.58g due to inclusion of a single active LRF. The activity of the LRF is complementarily supported by seismic source property studies, including relocated hypocenters, clustering results, repeating events analysis and focal mechanisms of earthquakes in the past 20 years (Li et al., 2018). When incorporated with the above geological surveys, the seismicity distribution indicates an 8 - 10 km wide, right-lateral, NNE dipping fault zone along the eastern segment of the mapped LRF surficial trace (Figure 1) (Li et al., 2018). The seismicity relocation study (Li et al., 2018) further suggests that the active structure in this region should be interpreted as a step-over fault system consisting of two fault segments: the LRF to the north as well as the Southern Whidbey Island fault (SWIF) to the south. Under the rupture scenario of an earthquake nucleated on the LRF jumping across the step-over and propagating onto the SWIF, the current SW British Columbia seismic hazard model would significantly underestimate the extent of potential damage.

Previous numerical simulations of fault step-overs (e.g. Harris et al., 1991; Hu et al., 2016) demonstrate that earthquake rupture can jump across a step-over system under one of the following three scenarios: 1) a break-away rupture which propagates across the receiver fault surface completely, 2) a self-arresting rupture that propagates onto the receiver fault but stops shortly afterwards, or 3) no rupture jumping when the earthquake rupture stops at the source fault and fails to nucleate on the receiver fault. The break-away rupture is considered the most devastating as it produces the largest rupture size.

Whether earthquake ruptures can jump successfully across a step-over depends on a number of parameters, including the offset distance separating the source from the receiver fault (Harris & Day, 1999; Wesnousky, 2006; Hu et al., 2016), initial stress level on both faults (Hu et al., 2016), the free surface effect (Kase & Kuge, 2001; Hu et al., 2016), and fault burial depth (Kase & Kuge, 2001). A large offset distance impedes rupture jumping as stress perturbations radiated from rupture on the source fault decays with distance. A higher initial stress level on the source fault can generate stronger stress perturbations, while a higher initial stress level on the receiver fault increases its propensity to be triggered. Both factors contribute to promoting rupture jumping over the discontinuity. Besides, the Earth's surface, a traction-free boundary, can also promote rupture jumping as energy reflected from the free surface is capable of generating strong stress perturbations and sometimes supershear ruptures (Kase & Kuge, 2001; Chen & Zhang, 2006). Through a series of 3D simulations in a half-space model, Hu et al. (2016) found that the supershear rupture induced by the free surface can drive the rupture to jump over a distance > 10 km. They also report that rupture jumping distance significantly decreases with the fault burial depths (Kase & Kuge, 2001). It should be noted that earthquake rupture jumping scenario is collectively dependent on a range of factors, despite all these previous modelling efforts on the influence of different single parameters.

Rupture on the source fault will radiate and impact stress perturbations on the receiver fault. While the radiated stress perturbations directly control rupture scenarios, target model parameters (i.e. offset distance, fault initial stress level, and fault burial depth) exert their influence indirectly by resulting in different stress perturbations on the receiver fault. To inspect the stress perturbations induced by the source fault rupture, previous studies on fault step-over systems (Harris et al., 1991; Harris & Day, 1993; Fliss et al., 2005) propose the concept of stress difference $\Delta s(t)$:

$$\Delta s(t) = \mu_s \left|\sigma_{n0} + \Delta\sigma_n(t)\right| - \left|\tau_0 + \Delta\tau(t)\right| \tag{1}$$

where μ_s is the static frictional coefficient, σ_{n0} is the initial normal stress, $\Delta\sigma_n(t)$ denotes the time-dependent normal stress perturbation, τ_0 is the initial shear stress and $\Delta\tau$(t) denotes the time-dependent shear stress perturbation. Rupture can potentially occur when and where the stress difference is less than zero. A more recent example is from Hu et al. (2016), where they used $\Delta s(t)$ to explain that rupture jumping across distances greater than 10 km could only occur in lower normal stress cases with the free surface effect considered. It is noteworthy that the stress perturbations presented in previous studies were first calculated in simulations consisting of a single source fault, and then projected on a receiver fault plane in the step-over system. They considered that rupture will nucleate on the receiver fault when and where $\Delta s(t) < 0$, but did not make further quantitative assessment of whether the rupture will remain as self-arresting or develop into a break-away one.

In this study, we present 3D finite-element simulations of rupture process in the LRF step-over system. The first objective of this work is to study whether a rupture nucleated on the LRF will jump across the discontinuity and propagate onto the SWIF. We focus on the effect of offset distance, fault initial stress level and fault burial depth. The second objective is to identify keystone parameters that can collectively represent the influence of aforementioned variables and systematically study how they affect rupture jumping scenarios. We define the Over Stressed Zone (OSZ) as the region on the receiver fault plane with $\Delta s(t) < 0$ and use it to predict rupture scenarios on the receiver fault. The OSZ can be considered as an equivalence to the nucleation patch used to initiate an earthquake rupture on the receiver fault. Similar to previous work on modeling dynamic earthquake ruptures based on a linear slip-weakening law (Duan & Oglesby, 2006; Dalguer & Day, 2009; Galis et al., 2015; Xu et al., 2015; Harris et al., 2018), we conjecture that the variation of the OSZ size and the initial stress level on the receiver fault will have the most critical influence on rupture evolution. Following the convention used in previous studies (e.g. Xu et al., 2015), we characterize the OSZ size using its effective radius R_e:

$$R_e = \sqrt{\frac{A}{\pi}} \tag{2}$$

where A is the cumulative area of grids where $\Delta s(t) < 0$. We vary the values of target step-over parameters and observe the change of R_e resulted on the SWIF. Subsequently, we inspect the relationship between the R_e variation and the development of jumping scenarios. As we demonstrate later, the initial stress level on the receiver fault and R_e can be used to represent the joint influence of multiple model parameters. Different model parameters will result in different R_e values and consequently different rupture scenarios on the SWIF. Seismic moment on the SWIF will grow with increasing R_e. After R_e reaches a critical value dependent on the receiver fault initial stress level, the SWIF rupture becomes break-away.

2 Model Setup and Parameters

2.1 Step-over fault geometry, numerical method and parameters

Figure 2 shows the geometrical parameters of the LRF step-over system. Previous LRF seismicity relocation study (Li et al., 2018) provides some constraints on the LRF geometry parameters, including its fault dimension and dipping angle. Relocated seismicity suggests that the seismically active part of the fault has a length of $L_1 = 50$ km, extending to 30 km in depth with a dip angle of $\theta_1 = 60^o$, therefore its along-dip dimension is determined as $W_1 = 34.6$ km. The SWIF geometry, however, is relatively poorly resolved. Relocated microseismicity studies (Li et al., 2018; Savard et al., 2018) indicate that the SWIF could extend to 30 km in depth, but there is no information to decisively determine its dip angle θ_2, length L_2, width W_2 as well as its offset distance L_0 from the LRF. Other studies provide some insights that the SWIF should be considered as a fault zone extending >150 km along strike from the Vancouver Island to the northern Puget Lowland (Sherrod et al., 2008), and it is a steeply NNE dipping fault zone as wide as 6 - 11 km (e.g. Johnson et al., 1999). In this work, for simplicity, we consider the SWIF segment in the proximity to the LRF with $\theta_2 = 90^o$, $L_2 = 30$ km and $W_2 = 30$ km. The offset distance L_0 is varied from 1 to 10 km to study its effect on rupture jumping scenarios. The along-strike overlapping distance L is set as 10 km as relocated seismicity suggests it falls within the range between 5 and 15 km.

As there is no definitive geological evidence on whether the LRF or the SWIF reaches the surface, the possibility of faults with nonzero burial depths cannot be excluded. Considering surficial fault scarps observed along the LRF (Morell et al., 2017) and the abundance of crustal LRF earthquakes at shallow depths <5 km (Li et al., 2018), it is reasonable to assume the burial depth of the LRF (D_1) is relatively shallower. Since Li et al. (2018) illustrate the SWIF lacks earthquakes shallower than 5 km, the burial depth of the SWIF (D_2) is likely deeper than the LRF. We will vary D_1 within the range of [0, 1, 2] km and D_2 within the range of [0, 5, 10] km to study their effects. A complete list of parameters discussed in this study, and their values are included in Table 1.

We use Pylith, a finite-element code for 3D dynamic earthquake rupture simulations (Aagaard et al., 2013) to investigate rupture process in the LRF step-over system. We consider the LRF and the SWIF as two planar faults embedded in a homogeneous, isotropic elastic half-space: P- and S- wave speeds are: $V_p = 6000$ m/s and $V_s = 3464$ m/s, Poisson's ratio $\nu = 0.25$, and shear modulus $G = 32$ GPa. Fault frictional property is described by a linear slip-weakening law (Ida, 1972), where the frictional coefficient μ decreases linearly from a static value μ_s to a dynamic value μ_d with slip distance δ over a characteristic slip-weakening distance d_0:

$$\mu(\delta) = \begin{cases} \mu_s - (\mu_s - \mu_d)\,\delta/d_0, & \delta \le d_0 \\ \mu_d, & \delta > d_0 \end{cases} . \tag{3}$$

With these notations, static and dynamic shear stresses are thus defined as $\tau_s = \mu_s \sigma_{n0}$ and $\tau_d = \mu_d \sigma_{n0}$, respectively. The initial shear stress τ_0 can be represented using the nondimensional value (Andrews, 1976):

$$S_0 = \frac{\tau_s - \tau_0}{\tau_0 - \tau_d} \tag{4}$$

A smaller S_0 indicates that the fault is closer to failure. It has been denoted that a sufficiently small S_0 can induce break-away or even supershear ruptures in a full space model (Xu et al., 2015). We assume a homogeneous distribution of initial shear stress on the fault planes, except that the initial shear stress on the nucleation patch (τ_0^i) is assumed to be slightly higher than the yielding strength (i.e. static shear stress τ_s) for rupture initialization (Table 1). In most cases considered in this study, we assume that both fault segments in the step-over system have the same initial shear stress τ_0, and use S_0 to represent the initial stress levels on both faults. We use S_0^{LRF} and S_0^{SWIF} to discriminate S_0 on the LRF and the SWIF, if necessary, for example, when we investigate cases with different initial stress levels on two faults or we focus on the influence of the initial stress level on the SWIF.

The cohesive zone size follows the definition in Day et al. (2005):

$$\Lambda_0 = \frac{9\pi}{32} \frac{G}{1-\nu} \frac{d_0}{\tau_s - \tau_d}. \tag{5}$$

$\Lambda_0 \approx 1.5$ km with parameter values chosen in our study (Table 1), which is about 10 times of the model grid size of 0.15 km, satisfying the numerical resolution requirement (Day et al., 2005). To ensure computational stability, the computation time step Δt is set to be much smaller than the time it takes for P wave to travel across the shortest grid size. Besides, distorted tetrahedral grids in the mesh require smaller time steps due to artificially high stiffness resulting from distorted shape (Aagaard et al., 2017). For a given grid, the critical time step Δt_{cr} is derived from the formula given in Aagaard et al. (2017):

$$\Delta t_{cr} = \frac{V_p}{\min(e_{\min}, C\frac{3V}{\sum_{i=1}^{4} A_i})} \tag{6}$$

where e_{min} is the shortest grid size, V is the cell volume, A_i denotes the area of the i^{th} face, and C is the scaling factor empirically determined as 6.38 (Aagaard et al., 2017). The global minima of Δt_{cr} is calculated to be 0.009 s. Therefore, time step Δt is set as 0.005 s in this study.

2.2 Numerical experiment setup

We will first inspect how different parameters of the step-over system will affect the effective radius of the OSZ—R_e—observed on the SWIF. Second, we investigate the effect of these parameters on rupture jumping scenarios. To accomplish this, two sets of simulations are performed: 1) simulations considering the rupture on the single LRF; and 2) simulations considering ruptures on both faults in the step-over system. In the first set , which can be referred as the single LRF simulation set, we simulate dynamic ruptures on the single LRF (the only fault that rupture is simulated), and project induced stress perturbation tensor on a hypothetical plane with the same geometrical parameter as the SWIF. Rupture is not simulated on the hypothetical plane and it only serves as a placeholder to receive the stress perturbations induced by the LRF rupture. We define the OSZ as the region on the hypothetical plane where stress difference $\Delta s(t) < 0$, and its area can be obtained by summing up all triangular mesh surface areas satisfying $\Delta s(t) < 0$. This treatment allows us to focus attention to the stress perturbations radiated from the source fault. In the second set, which can be referred as the step-over simulation set, we simulate dynamic earthquake ruptures in the Leech River step-over system with both faults present, and study the effects of different model parameters on the final SWIF rupture scenarios.

3 Simulation results

Through the implementation of two aforementioned simulation sets, we intend to interpret the influence of different parameters on final rupture jumping scenarios, a response represented by R_e on the SWIF with the initial stress level of S_0^{SWIF} to stress perturbations radiated from the LRF. A theoretical estimate on the critical nucleation size for break-away ruptures on an unbounded fault is developed by Galis et al. (2015):

$$R_{cr} = \frac{\pi}{4} \frac{1}{f_{\min}^2} \frac{\tau_s - \tau_d}{(\tau_0 - \tau_d)^2} G d_0 \tag{7}$$

where R_{cr} is the critical nucleation radius and $f_{\min}$ is the the minimum of the function

$$f(x) = \sqrt{x} \left[1 + \frac{\tau_0^i - \tau_0}{\tau_0 - \tau_d} (1 - \sqrt{1 - 1/x^2}) \right] \tag{8}$$

where τ_0^i is the initial shear stress within the nucleation patch and τ_0 and τ_d are the initial shear stress and dynamic shear stress defined outside of the nucleation patch. We verify our numerical simulations against the theoretical estimates by simulating ruptures on a single fault with the same geometry as SWIF through nucleation within a manually prescribed OSZ with a given R_e; here R_e is effectively the prescribed nucleation zone size. Its location is fixed at the fault plane center for simplicity. The consistency achieved between this comparison (Figure 3) suggests that we can focus discussion on the influence of R_e and S_0^{SWIF} on SWIF rupture scenarios.

For the convenience of discussions in subsequent subsections, we will first describe how the OSZ on a hypothetical SWIF fault plane evolves with time as rupture develops on the LRF in Section 3.1. In Sections 3.2-3.4, we present the influence of different step-over parameters on the OSZ size and final jumping scenarios as rupture is simulated on both faults.

3.1 Time evolution of OSZ on SWIF

Figure 4 shows the development of the OSZ resulted on a hypothetical SWIF fault plane for a simulation with initial shear stress level $S_0 = 0.7$ on both faults, offset distance $L_0 = 1$ km, and burial depths $D_1 = 0$ km and $D_2 = 0$ km. The initial rupture nucleated on the LRF is sub-shear. When the rupture front reaches the free surface, a super-shear rupture is generated by the energy reflected from the free surface ($t = 9$ s in Figure 4a). These two rupture fronts are spatially separated due to different propagation speeds. In comparison, for a higher LRF initial stress level (lower $S_0 = 0.5$) with other parameters fixed, the initial rupture develops into a super-shear rupture before reaching the free surface ($t = 4$ s in Figure 5a). When the initial rupture front meets the free surface, an additional super-shear rupture is also generated, which is embedded in the initial rupture. It is clear from Figures 4b and 5b that the shape of the OSZ is irregular, and there could be multiple, separate OSZ patches simultaneously triggered on the receiver fault. In the following analysis, only R_e of the largest OSZ patch is considered, as a break-away rupture will be triggered as long as the largest OSZ reaches the critical size.

Figure 6 summarizes the time evolution of the effective size of the OSZ under the two initial stress levels for the cases in Figure 4 and 5. For a lower S_0, the OSZ starts to appear earlier (t $\sim$ 10 s) than the higher S_0 case (t $\sim$ 13 s). The OSZ also remains larger throughout the entire process, with the maximum R_e at $\sim$ 3.5 km and $\sim$ 2.5 km respectively. It is evident that a lower initial stress on one fault segment in a step-over system provides more favorable conditions for nucleating ruptures on the other segment, with all other parameters held constant. For each simulation case, we take the time-averaged $\overline{R_e}$ as a representation of the OSZ size for discussion in the following sections.

3.2 Influence of initial stress level

In this section we focus on the effects of initial stress levels of LRF and/or SWIF on the size of the OSZ resulted on the SWIF. Here we fix the offset distance $L_0 = 1$ km, burial depths $D_1 = D_2 = 0$ km. Effects of these parameters will be examined in Sections 3.3 and 3.4. In general, we observe larger average OSZ size $\overline{R_e}$ at lower S_0 values. In other words, rupture is more likely to be nucleated on SWIF when the initial stress level is high (closer to static stress) on either or both of the LRF and SWIF faults. For example, as shown in the first panel of Figure 7, when the initial stress level is low ($S_0 >= 1.1$), $\overline{R_e}$ drops to a value significantly lower than R_{cr}. This can be directly compared with rupture jumping scenarios obtained in the step-over simulations (Figure 10). Simulation results show that a break-away rupture cannot develop on the SWIF when $S_0 \geq 1.1$: rupture may propagate onto the SWIF, but will get arrested shortly, indicating limited seismic hazards. The last two panels in Figure 7 illustrate the influence of initial stress level on one fault when S_0 on the other fault is fixed at 0.5. Based on these two panels, we can interpret the influence of S_0 in two aspects. First, a higher initial stress level on the SWIF indicates that it is prone to failure (smaller R_{cr}) and leads to a lager $\overline{R_e}$ (the second panel in Figure 7), both encouraging rupture jumping across the discontinuity. Second, a higher initial stress level on the LRF will radiate stronger stress perturbations and larger OSZs on the SWIF (the third panel in Figure 7).

3.3 Influence of offset distance

Figure 8 illustrates the influence of the offset distance between the LRF and the SWIF on the OSZ size resulted on the SWIF, at various initial stress levels. For each caes, S_0 is assumed to be the same on both faults. This figure shows that $\overline{R_e}$ declines approximately linearly with the increase of L_0, demonstrating weaker stress perturbations the SWIF receives when the two faults are further apart. This is consistent with the results of numerical experiment that a larger offset distance discourages the development of break-way ruptures (Figure 10) when other parameters are fixed. We define the maximum jumping distance as the largest offset distance that allows a self-arresting rupture on the SWIF, and the critical jumping distance as the largest offset distance that allows a break-away rupture on the SWIF. Rupture jumping distance reaches its maximum of 8 km when the SWIF has sufficient proximity to its failure (low $S_0 = 0.5$) and the LRF reaches the free surface ($D_1 = 0$ km in Figures 10a-10b). For simulations with $S_0 = 0.7$, $D_1 = 0$ km, and $D_2 = 0$ km, $\overline{R_e}$ drops below the corresponding R_{cr} when L_0 increases to 3 km or larger (Figure 8). The shrinkage of OSZ with increasing offset distance results in a critical jumping distance of 2 km (Figure 10a).

A previous numerical study (Hu et al., 2016) suggests that the critical jumping distance can reach up to 14 km, significantly exceeding the largest critical jumping distance of 6 km obtained in this work ($S_0 = 0.5$, $D_1 = 0$ km and $D_2 = 0$ km in Figure 10a). This discrepancy can be contributed to two factors. First, they used a higher initial stress level of $S_0 = 0.4$, which facilitates rupture jumping as well as the development of break-away ruptures. Second, the acceleration length of rupture front (ALRF) on the source fault prior to rupture jumping—the distance between the source fault nucleation patch and its fault edge in the proximity of the step-over—used in Hu et al. (2016) is 34 km, larger than the ALRF of 20 km used in our work. A larger ALRF leads to higher slip gradients on the source fault, hence stronger stopping phases and a larger critical jumping distance (Oglesby, 2008; Elliott et al., 2009).

3.4 Influence of fault burial depth

The influence of fault burial depth (i.e. D_1 and D_2) on $\overline{R_e}$ is demonstrated in Figure 9. Overall we observe the strongest perturbation effects when both faults reach the free surface. The OSZ size decreases with the burial depths of either fault. When the LRF is a blind fault ($D_1 > 0$), the energy reflected by the free surface diminishes as the burial depth increases, resulting in weaker stress perturbations and smaller OSZs on the SWIF. The weakening of stress perturbation radiated on the SWIF is also observed when increasing D_2 while keeping $D_1 = 0$ km. It takes effect in a different way than increasing D_1: a nonzero D_1 weakens the stress perturbations from the source side while a nonzero D_2 weakens the stress perturbations from the receiver side. It can also be speculated from Figure 9 that the effect of a larger D_1 can be compensated by a smaller D_2. Thus, it may be problematic to predict the jumping scenario by measuring the burial depth of either the source fault or the receiver fault alone. For a given D_1, $\overline{R_e}$ keeps decreasing with the deepening of the receiver fault burial depth—D_2, indicating stress perturbations radiated on the receiver fault is a near-surface effect. The OSZ may be completely diminished when the receiver fault is too deep even the source fault rupture reaches the free surface. The effect of nonzero D_2 in impeding rupture jumping, however, is much less effective compared to D_1. Figures 10a-10b show the earthquake rupture is still capable of jumping over a distance of 8 km when D_2 increases to 5 km with other parameters fixed as $L_0 = 1$ km, $S_0 = 0.5$, and $D_2 = 0$km. Figure 5b shows the OSZ developed on the SWIF can extend down to about 12 km (the snapshot at t = 18 s in Figure 5b), indicating the SWIF earthquake will be triggered when D_2 is shallower than this depth.

3.5 Simulation results summary

The general messages delivered in Figures 6-9 are : 1) the OSZ enlarges to its peak size a few seconds after its first appearance and shrinks gradually; and 2) higher initial stress levels, closer offset distances and shallower fault burial depths produce larger OSZs on the receiver fault. These messages are consistent with the phase diagrams showing the influence of different parameters on final rupture scenarios in Figure 10. It is illustrated clearly that higher initial stress levels, smaller offset distances or shallower fault burial depths will promote successful rupture jumping and the transition of self-arresting ruptures into break-away ones. The final rupture jumping scenario depends on the collective influence of various model parameters, which can be interpreted by inspecting how they change R_e on the SWIF and whether R_e reaches R_{cr}. The phase diagrams in Figure 10 can be useful to predict final rupture jumping scenarios with given parameter values. Based on relocated seismicity (Li et al., 2018), it is most likely that the SWIF has a burial depth of $D_2 = 5$ km and the offset distance $L_0 = 5$ km. Based on Figure 10b, it can be inferred that a rupture nucleated on the LRF is unlikely to jump across the step-over even when the LRF rupture reaches the free surface ($D_1 = 0$ km), unless the two faults are critically stressed ($S_0 = 0.5$).

From the initial comparative simulations with a single SWIF in Section 3, we obtain the data of the final seismic moment on the SWIF (M_0^{SWIF}) as a function of R_e for different initial stress levels, which we denote as the (R_e, M_0^{SWIF}) data set. We then obtain the data of the OSZ development history (represented by $\overline{R_e}$) resulting from the single LRF simulation set and seismic moment on the SWIF (M_0^{SWIF}) resulting from the step-over simulation set, which we denote as the ($\overline{R_e}$, M_0^{SWIF}) data set. We create Figure 11 by combining these two data sets, intending to compile and compare the results of different simulation sets. Both data sets follow the trend that : 1) a larger R_e or $\overline{R_e}$ leads to a larger M_0^{SWIF}; and 2) when R_e or $\overline{R_e}$ reaches a critical value, the SWIF rupture becomes break-away and its seismic moment increases up to a saturated value depending on the available rupture area of the receiver fault. The critical value for both R_e and $\overline{R_e}$ can be estimated by Equation 7 and illustrated by a vertical dashed line for each S_0 case in Figure 11. The consistency in Figure 11 demonstrates that $\overline{R_e}$ and S_0^{SWIF} are the keystone variables directly controlling final rupture jumping scenarios in a step-over fault system, while different parameters exert their influence on rupture scenarios by resulting in different OSZ sizes. Some discrepancies should be noted: the earthquake rupture in the ($\overline{R_e}$, M_0^{SWIF}) data set produces slightly higher seismic moments and can develop into a break-away rupture with a relatively smaller OSZ size (Figures 11a and 11c). We speculate that these discrepancies can be contributed to that the OSZ radiated on the SWIF in a step-over system usually reaches the free surface (Figures 4b and 5b). This will introduce an extra energy kick from the free surface compared to the cases in the initial comparative simulations, especially when the rupture in the comparative simulations does not expand to the free surface with a small R_e.

4 Discussion

4.1 Stopping phases

In our simulations, the fault edges are set as unbreakable boundaries except the boundary reaching the free surface when $D_1 = 0$ km or $D_2 = 0$ km. Rupture fronts meeting the unbreakable fault edges will be terminated abruptly. This abrupt termination will produce significantly high co-seismic slip gradients near the boundary and radiate high frequency seismic energy—stopping phases (Bernard & Madariaga, 1984). Previous numerical results (Oglesby, 2008) illustrate that the possibility of rupture jumping is suppressed when reducing the gradients of the initial shear stress distribution near the fault boundary. In addition, through the analysis of historical large-magnitude earthquakes, Elliott et al. (2009) reveal that it is unlikely for a rupture to propagate onto the next segment for earthquakes with low slip gradients near the step-overs. Both studies recognize the indispensability of seismic energy from the stopping phases in promoting earthquake jumping across the step-over.

As shown in Figures 4 and 5, the OSZ starts to develop after the right-ward propagating LRF rupture reaches the right fault edge in the proximity of the step-over. The vertical red dashed lines in Figure 6 represent when the LRF rupture fronts meet the fault edge in the proximity of the step-over for the simulation case in Figure 4 (simulation snapshots at t = 12 s and t = 13.7 s). Curves for $S_0 = 0.7$ in Figure 6 include two pulses, representing the energy from the termination of two rupture fronts, respectively. These transient properties serve as an indicator of the passage of stopping phases and its role in radiating stress perturbations on the SWIF.

Rupture propagation of 2 selected simulations are included in the supplementary materials as Movies S1-S2. Rupture on the SWIF starts to propagate after the source fault rupture front reaches the right edge of the LRF, an unbreakable boundary halting rupture propagation. This indicates the strong effect of stopping phases. Movies S1-S2 also show that the SWIF hypocenter is about 10 km from its left boundary, which corresponds to the projection of the LRF right fault boundary on the SWIF surface. King et al. (1994) calculated the static stress changes due to the slip on a right-lateral master fault in an extensional step-over system. Their study suggests that, for a right-lateral fault with a strike parallel to the source fault, positive Coulomb stress changes are distributed in the proximity of the source fault boundary, which is consistent with our observations on the SWIF hypocenter location.

4.2 Fault stress level initialization

The initialization of shear stress on the fault is a crucial component of a dynamic rupture simulation study. For simplicity, we assume a uniform distribution of initial stress across two planar faults (Harris et al., 1991; Kase & Kuge, 2001; Xu et al., 2015; Weng & Yang, 2017), except for the stress asperity implemented to initialize the rupture. While the reduced complexity allows us focus on target parameters, previous studies have shown the undeniable significance of other stress initialization strategies: 1) Regional tectonic stress strategy (Fliss et al., 2005; Bhat et al., 2007); 2) Fault roughness strategy (Dunham et al., 2011; Mai & Beroza, 2002); and 3) Evolved stress strategy (Stern, 2016; Tarnowski, 2017). In Fliss et al. (2005) and Bhat et al. (2007), regional tectonic stress tensor is resolved onto the fault plane according to local surface normal orientations. This strategy can be used to inspect the fault's geometrical effects. Based on an observation of the orientation $S_{H_{\max}}$, a stress tensor is created with the assumption of a σ_1 direction and

S_0. Besides, observational studies suggest that fault roughness exists at all scales across the surface (Dunham et al., 2011; Mai & Beroza, 2002) in the aspect of heterogeneous fault asperities strength distributions and fault surface non-planarity. Fault roughness has been demonstrated to constitute a fundamental factor of the rupture process (Mai & Beroza, 2002; Brodsky et al., 2016). For example, in Zielke et al. (2017)'s numerical simulations, it is shown that the release of seismic moment can vary widely depending on the roughness and the location of strength asperities. Moreover, in our 3D dynamic simulations, we ignore the process of stress loading on the faults. It is suggested that a more realistic initial stress distribution for dynamic simulations can be constructed from the stress outputs from quasi-static crustal modelling (Stern, 2016; Tarnowski, 2017) or from the geodetic loading conditions (Yang et al., 2019). But this strategy requires rigorous pre-calculations of the fault stress evolution history in designated study areas. The lack of necessary observations, e.g., fault roughness data and stress evolution history, prevents us from implementing other strategies. In addition, the implementation of the regional stress tensor strategy becomes unnecessary as the influence of fault geometrical irregularities is currently beyond the scope of this study. When data is available, our work can be expanded to investigate the influence of these factors on the rupture process in a step-over system.

4.3 Seismic hazards assessment

This study reveals potential limitations of previous LRF seismic hazard studies based on ground motion simulations (Molnar et al., 2014) and probabilistic seismic hazard analysis (Kukovica et al., 2019), which only consider the influence of a single LRF. Figure 12a shows, if an earthquake propagates across the offset and continues onto SWIF as a break-way rupture(for example as in the case of $S_0 = 0.5$, $S_0 = 0.7$ and $S_0 = 0.9$), the final seismic moment could increase by 25%. In an observational study on the 1997 M_w 7.1 Harnai (Parkistan) earthquake (Nissen et al., 2016), the eventual seismic moment is increased by 50% due to the successive rupture triggered on the receiver fault by the source fault rupture. Fault models derived by Nissen et al. (2016) using InSAR data suggest that the surface projection of these two faults is parallel with an offset distance of ~ 5 km. Both studies demonstrate the importance of considering the possibility of rupture jumping for regional seismic assessment. M_0^{SWIF} released by a self-arresting rupture on the SWIF ($S_0 = 1.1$ and $S_0 = 1.3$) is negligible therefore not shown in Figure

12a. The moment release rate ($\dot{M}_0$) as a function of time in Figure 12b displays more details on the energy release history, which highlights the difference between a self-arresting ruputre and a break-away one. The $\dot{M}_0$ curves for self-arresting ruptures (dashed lines) are single-peaked while the $\dot{M}_0$ curves for break-away ruptures (solid lines) have double peaks. The second peak represents the successive fault rupture on the SWIF. Similar patterns of multiple $\dot{M}_0$ pulses have been observed in several multi-fault earthquakes for example the 1997 Harnai earthquake (Nissen et al., 2016) and the 2016 Kaikoura earthquake (Hollingsworth et al., 2017).

In the state-of-the-art rupture forecasts model in California—UCERF3 (Field et al., 2014), the possibility of rupture jumping between fault segments separated by a distance >5 km is not considered. This assumption, however, is not definitively solid as sequential failure of two faults with offset distance larger than 5 km could happen under many conditions, e.g., when the receiver fault is critically-stressed, or the free surface effect is strong enough. Therefore, the seismic hazards of a step-over fault system such as the LRF-SWIF can be significantly underestimated if the possibility of jumping distance >5 km is neglected.

Furthermore, it is questionable to rely on the offset distance alone to judge whether an earthquake will jump across the discontinuity. First, whether an earthquake rupture jumps across the discontinuity is a collective result depending on a variety of model parameters (i.e., L_0, S_0, D_1, D_2). Second, the offset distance is not always observable especially when there is a lack of the observation of surficial fault scarps. Based on seismicity relocation and finite fault slip model, Ross et al. (2019) determined that the 2019 Ridgecrest earthquake ruptured multiple crustal faults with significant geometrical complexity. Most of the faults ruptured in this earthquake sequence are not mapped in previous fault databases.

4.4 Aftershock pattern predictions

It has been a common practice to relate near-field aftershock distributions or seismicity triggering with static stress changes due to permanent displacement (Toda et al., 1998; Verdecchia et al., 2018). In a broader sense, aftershock triggering mechanism can be treated as a problem of stress transfer from the primary fault to micro-faults in the proximity. Our findings, especially the transient properties of the OSZ, highlight the nonnegligible effects of dynamic stress changes in the near-field. Aftershocks could also be triggered in a stress shadow zone—regions with zero or negative static stress changes, as long as the transient dynamic stress perturbations are capable of bringing it to failure. Besides, separating dynamic and static stress changes in the near-field is impossible. Voisin et al. (2004) suggest the complete Coulomb failure function, a combination of static and dynamic stress changes, should be considered to explain seismicity triggering mechanisms and aftershock patterns.

5 Conclusions

We conduct a suite of numerical simulations to study the conditions under which an earthquake can jump across the Leech River fault step-over system. Whether a rupture jumps across the discontinuity and whether it develops into a break-away or self-arresting rupture depend on the collective effects of a variety of parameters. Therefore, it may be not always feasible to predict whether rupture jumping is possible based on a single parameter. Instead, we propose and verify through dynamic rupture simulation that the final rupture jumping scenarios can be interpreted as the response of the SWIF to stress perturbations radiated from the LRF rutpure, which can be quantified using the Over Stressed Zone (OSZ) size—R_e. We find R_e and the the receiver fault initial stress level (S_0^{SWIF}) are the keystone variables that can represent the collective influence of various parameters. Specifically, a smaller offset distance (L_0), a higher initial shear stress level (S_0) or a shallower burial depth (D_1 or D_2) will lead to a larger R_e resulted on the SWIF. The SWIF seismic moment increases with increasing R_e. When R_e reaches the critical value dependent on S_0^{SWIF}, the rupture becomes break-away on the SWIF and its seismic moment increasese up to a saturated value depending the available rupture area of the receiver fault. Our study suggests that the seismic hazards posed by the LRF system could be significantly higher than previously expected, especially when earthquake nucleated on the LRF jumps onto the SWIF as a break-away rupture.

Acknowledgments

The open-source software PyLith used in this study is available from the Computaional Infrastructure for Geodynamics at https://geodynamics.org/cig/software/pylith/. All data are synthetic from numerical simulations. This work is supported by the Natural

Sciences and Engineering Research Council of Canada Discovery Grant RGPIN-2018-05389 to Y. Liu at McGill University.

References

Aagaard, B. T., Knepley, M. G., & Williams, C. A. (2013). A domain decomposition approach to implementing fault slip in finite-element models of quasi-static and dynamic crustal deformation. *Journal of Geophysical Research: Solid Earth*, *118*(6), 3059–3079.

Aagaard, B. T., Knepley, M. G., & Williams, C. A. (2017). PyLith User Manual, Version 2.2.1. Davis, CA: Computational Infrastructure of Geodynamics. Retrieved from `geodynamics.org/cig/software/github/pylith/v2.2.1/pylith-2.2.1_manual.pdf`

Andrews, D. (1976). Rupture velocity of plane strain shear cracks. *Journal of Geophysical Research*, *81*(32), 5679–5687.

Barnhart, W. D., Hayes, G. P., & Gold, R. D. (2019). The July 2019 Ridgecrest, California, Earthquake Sequence: Kinematics of Slip and Stressing in Cross-Fault Ruptures. *Geophysical Research Letters*, *46*(21), 11859–11867.

Bernard, P., & Madariaga, R. (1984). A new asymptotic method for the modeling of near-field accelerograms. *Bulletin of the Seismological Society of America*, *74*(2), 539–557.

Bhat, H. S., Dmowska, R., Rice, J. R., & Kame, N. (2004). Dynamic slip transfer from the Denali to Totschunda faults, Alaska: Testing theory for fault branching. *Bulletin of the Seismological Society of America*, *94*(6B), S202–S213.

Bhat, H. S., Olives, M., Dmowska, R., & Rice, J. R. (2007). Role of fault branches in earthquake rupture dynamics. *Journal of Geophysical Research: Solid Earth*, *112*(B11).

Brodsky, E. E., Kirkpatrick, J. D., & Candela, T. (2016). Constraints from fault roughness on the scale-dependent strength of rocks. *Geology*, *44*(1), 19–22.

Cesca, S., Zhang, Y., Mouslopoulou, V., Wang, R., Saul, J., Savage, M., ... Dahm, T. (2017). Complex rupture process of the Mw 7.8, 2016, Kaikoura earthquake, New Zealand, and its aftershock sequence. *Earth and Planetary Science Letters*, *478*, 110–120.

Chen, X., & Zhang, H. (2006). Modelling rupture dynamics of a planar fault in 3-D half space by boundary integral equation method: An overview. *pure and applied geophysics*, *163*(2-3), 267–299.

Dalguer, L. A., & Day, S. M. (2009). Asymmetric rupture of large aspect-ratio faults at bimaterial interface in 3D. *Geophysical Research Letters*, *36*(23).

Day, S. M., Dalguer, L. A., Lapusta, N., & Liu, Y. (2005). Comparison of finite difference and boundary integral solutions to three-dimensional spontaneous rupture. *Journal of Geophysical Research: Solid Earth*, *110*(B12).

Duan, B., & Oglesby, D. D. (2006). Heterogeneous fault stresses from previous earthquakes and the effect on dynamics of parallel strike-slip faults. *Journal of Geophysical Research: Solid Earth*, *111*(B5). doi: 10.1029/2005JB004138

Dunham, E. M., & Archuleta, R. J. (2004). Evidence for a supershear transient during the 2002 Denali fault earthquake. *Bulletin of the Seismological Society of America*, *94*(6B), S256–S268. doi: 10.1785/0120040616

Dunham, E. M., Kozdon, J. E., Belanger, D., & Cong, L. (2011). Earthquake ruptures on rough faults. In *Multiscale and multiphysics processes in geomechanics* (pp. 145–148). Springer.

Duputel, Z., & Rivera, L. (2017). Long-period analysis of the 2016 Kaikoura earthquake. *Physics of the Earth and Planetary Interiors*, *265*, 62–66.

Eberhart-Phillips, D., Haeussler, P. J., Freymueller, J. T., Frankel, A. D., Rubin, C. M., Craw, P., … others (2003). The 2002 Denali fault earthquake, Alaska: A large magnitude, slip-partitioned event. *Science*, *300*(5622), 1113–1118.

Elliott, A., Dolan, J., & Oglesby, D. (2009). Evidence from coseismic slip gradients for dynamic control on rupture propagation and arrest through stepovers. *Journal of Geophysical Research: Solid Earth*, *114*(B2).

Field, E. H., Arrowsmith, R. J., Biasi, G. P., Bird, P., Dawson, T. E., Felzer, K. R., … others (2014). Uniform California earthquake rupture forecast, version 3 (UCERF3)—The time-independent model. *Bulletin of the Seismological Society of America*, *104*(3), 1122–1180.

Fliss, S., Bhat, H. S., Dmowska, R., & Rice, J. R. (2005). Fault branching and rupture directivity. *Journal of Geophysical Research: Solid Earth*, *110*(B6).

Galis, M., Pelties, C., Kristek, J., Moczo, P., Ampuero, J.-P., & Mai, P. M. (2015). On the initiation of sustained slip-weakening ruptures by localized stresses. *Geophysical Journal International*, *200*(2), 890–909. doi: 10.1093/gji/ggu436

Hamling, I. J., Hreinsdóttir, S., Clark, K., Elliott, J., Liang, C., Fielding, E., . . . others (2017). Complex multifault rupture during the 2016 Mw 7.8 Kaikōura earthquake, New Zealand. *Science*, *356*(6334), eaam7194.

Harris, R. A., Archuleta, R. J., & Day, S. M. (1991). Fault steps and the dynamic rupture process: 2-D numerical simulations of a spontaneously propagating shear fracture. *Geophysical Research Letters*, *18*(5), 893–896.

Harris, R. A., Barall, M., Aagaard, B., Ma, S., Roten, D., Olsen, K., . . . others (2018). A suite of exercises for verifying dynamic earthquake rupture codes. *Seismological Research Letters*, *89*(3), 1146–1162.

Harris, R. A., & Day, S. M. (1993). Dynamics of fault interaction: Parallel strike-slip faults. *Journal of Geophysical Research: Solid Earth*, *98*(B3), 4461–4472.

Harris, R. A., & Day, S. M. (1999). Dynamic 3D simulations of earthquakes on en echelon faults. *Geophysical Research Letters*, *26*(14), 2089–2092.

Hollingsworth, J., Ye, L., & Avouac, J.-P. (2017). Dynamically triggered slip on a splay fault in the Mw 7.8, 2016 Kaikoura (New Zealand) earthquake. *Geophysical Research Letters*, *44*(8), 3517–3525.

Hu, F., Zhang, Z., & Chen, X. (2016). Investigation of earthquake jump distance for strike-slip step overs based on 3-d dynamic rupture simulations in an elastic half-space. *Journal of Geophysical Research: Solid Earth*, *121*(2), 994–1006.

Johnson, S. Y., Dadisman, S. V., Childs, J. R., & Stanley, W. D. (1999). Active tectonics of the Seattle fault and central Puget Sound, Washington—Implications for earthquake hazards. *Geological Society of America Bulletin*, *111*(7), 1042–1053.

Kase, Y., & Kuge, K. (2001). Rupture propagation beyond fault discontinuities: significance of fault strike and location. *Geophysical Journal International*, *147*(2), 330–342.

King, G. C., Stein, R. S., & Lin, J. (1994). Static stress changes and the triggering of earthquakes. *Bulletin of the Seismological Society of America*, *84*(3), 935–953.

Kukovica, J., Ghofrani, H., Molnar, S., & Assatourians, K. (2019). Probabilistic Seismic Hazard Analysis of Victoria, British Columbia: Considering an Active Fault Zone in the Nearby Leech River Valley. *Bulletin of the Seismological Society of America*, *109*(5), 2050–2062.

Li, G., Liu, Y., Regalla, C., & Morell, K. D. (2018). Seismicity relocation and fault structure near the Leech River fault zone, southern Vancouver Island. *Journal of Geophysical Research: Solid Earth*, *123*(4), 2841–2855.

Liu, C., Lay, T., Brodsky, E. E., Dascher-Cousineau, K., & Xiong, X. (2019). Coseismic Rupture Process of the Large 2019 Ridgecrest Earthquakes From Joint Inversion of Geodetic and Seismological Observations. *Geophysical Research Letters*, *46*(21), 11820–11829.

Mai, P. M., & Beroza, G. C. (2002). A spatial random field model to characterize complexity in earthquake slip. *Journal of Geophysical Research: Solid Earth*, *107*(B11), ESE–10.

Massey, N., MacIntyre, D., Desjardins, P., & Cooney, R. (2005). Digital map of British Columbia: whole province. *BC ministry of energy and mines, GeoFile*, *1*.

Molnar, S., Cassidy, J. F., Olsen, K. B., Dosso, S. E., & He, J. (2014). Earthquake ground motion and 3D Georgia basin amplification in southwest British Columbia: Shallow blind-thrust scenario earthquakes. *Bulletin of the Seismological Society of America*, *104*(1), 321–335.

Morell, K. D., Regalla, C., Amos, C., Bennett, S., Leonard, L., Graham, A., ... Telka, A. (2018). Holocene Surface Rupture History of an Active Forearc Fault Redefines Seismic Hazard in Southwestern British Columbia, Canada. *Geophysical Research Letters*, *45*(21), 11,605-11,611. doi: 10.1029/2018GL078711

Morell, K. D., Regalla, C., Leonard, L. J., Amos, C., & Levson, V. (2017). Quaternary rupture of a crustal fault beneath Victoria, British Columbia, Canada. *GSA Today*, *27*(3), 4–10.

Nissen, E., Elliott, J., Sloan, R., Craig, T., Funning, G., Hutko, A., ... Wright, T. (2016). Limitations of rupture forecasting exposed by instantaneously triggered earthquake doublet. *Nature Geoscience*, *9*(4), 330–336.

Oglesby, D. (2008). Rupture termination and jump on parallel offset faults. *Bulletin of the Seismological Society of America*, *98*(1), 440–447.

Ross, Z. E., Idini, B., Jia, Z., Stephenson, O. L., Zhong, M., Wang, X., ... others (2019). Hierarchical interlocked orthogonal faulting in the 2019 Ridgecrest earthquake sequence. *Science*, *366*(6463), 346–351.

Savard, G., Bostock, M. G., & Christensen, N. I. (2018). Seismicity, metamorphism, and fluid evolution across the Northern Cascadia fore arc. *Geochemistry, Geophysics, Geosystems*, *19*(6), 1881–1897.

Sherrod, B. L., Blakely, R. J., Weaver, C. S., Kelsey, H. M., Barnett, E., Liberty, L., ... Pape, K. (2008). Finding concealed active faults: Extending the southern Whidbey Island fault across the Puget Lowland, Washington. *Journal of Geophysical Research: Solid Earth*, *113*(B5).

Stern, A. R. (2016). Fault Interaction within Restraining Bend Fault Systems.

Tarnowski, J. M. (2017). The Effects of Dynamic Stress on Fault Interaction and Earthquake Triggering in the San Gorgonio Pass and San Jacinto, CA Regions.

Toda, S., Stein, R. S., Reasenberg, P. A., Dieterich, J. H., & Yoshida, A. (1998). Stress transferred by the 1995 Mw = 6.9 Kobe, Japan, shock: Effect on aftershocks and future earthquake probabilities. *Journal of Geophysical Research: Solid Earth*, *103*(B10), 24543-24565. doi: 10.1029/98JB00765

Verdecchia, A., Pace, B., Visini, F., Scotti, O., Peruzza, L., & Benedetti, L. (2018). The role of viscoelastic stress transfer in long-term earthquake cascades: Insights after the central Italy 2016–2017 seismic sequence. *Tectonics*, *37*(10), 3411–3428.

Voisin, C., Cotton, F., & Di Carli, S. (2004). A unified model for dynamic and static stress triggering of aftershocks, antishocks, remote seismicity, creep events, and multisegmented rupture. *Journal of Geophysical Research: Solid Earth*, *109*(B6). doi: 10.1029/2003JB002886

Weng, H., & Yang, H. (2017). Seismogenic width controls aspect ratios of earthquake ruptures. *Geophysical Research Letters*, *44*(6), 2725-2732. doi: 10.1002/2016GL072168

Wesnousky, S. G. (2006). Predicting the endpoints of earthquake ruptures. *Nature*, *444*(7117), 358–360.

Xu, J., Zhang, H., & Chen, X. (2015). Rupture phase diagrams for a planar fault in 3-D full-space and half-space. *Geophysical Journal International*, *202*(3), 2194–2206.

Yang, H., Yao, S., He, B., Newman, A. V., & Weng, H. (2019). Deriving rupture scenarios from interseismic locking distributions along the subduction megathrust. *Journal of Geophysical Research: Solid Earth*, *124*(10), 10376–10392.

Zaleski, M. P. (2014). *Earthquake Loss Estimates, Greater Victoria, British Columbia* (Unpublished master's thesis). Simon Fraser University.

Zielke, O., Galis, M., & Mai, P. M. (2017). Fault roughness and strength heterogeneity control earthquake size and stress drop. *Geophysical Research Letters*, *44* (2), 777–783.

Table 1. List of simulation parameters

Parameter	Value
P wave velocity, V_p (m/s)	6000
S wave velocity, V_s (m/s)	3464
Poisson's ratio, ν	0.25
Shear modulus, G (GPa)	32
Static friction coefficient, μ_s	0.6
Dynamic friction coefficient, μ_d	0.2
Initial normal stress, σ_{n0} (MPa)	25
Static friction, τ_s (MPa)	15
Dynamic friction, τ_d (MPa)	5
Initial shear stress within the nucleation zone, τ_0^i (MPa)	16.5
Characteristic slip-weakening distance, d_0 (m)	0.4
LRF length, L_1 (km)	50
LRF width, W_1 (km)	34.6
LRF dip angle, θ_1	60^o
SWIF length, L_2 (km)	30
SWIF length, W_2 (km)	30
SWIF dip angle, θ_2	90^o
Overlapping distnace, L (km)	10
LRF burial depth, D_1 (km)	0 - 2
SWIF burial depth, D_2 (km)	0 - 10
Offset distance, L_0 (km)	1 - 10
Nondimensional fault initial shear stress level, S_0	0.5 - 1.5
LRF nucleation patch radius (km)	3

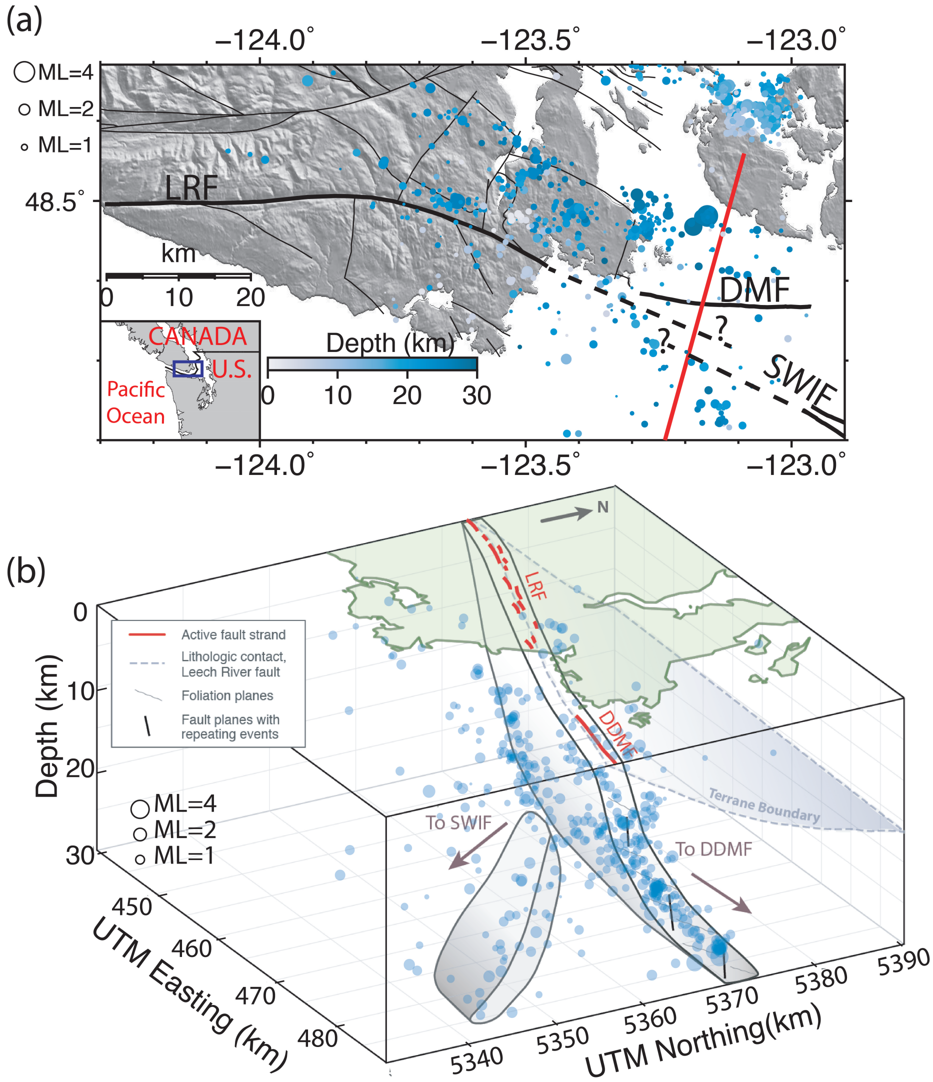

Figure 1. (a) Map of the study area showing relocated crustal earthquakes (depth <30 km) in Li et al. (2018), and mapped faults in British Columbia (Massey et al., 2005). The red line is the transect line in Figure 2b. Dashed lines represent possible extension from the LRF and the SWIF, respectively. The question marks indicate this configuration is based on educated guess with weak geological evidence. LRF: Leech River fault. SWIF: Southern Whidbey Island fault. DMF: Devils' Mountain fault. (b) Illustration of the LRF step-over system with 3D seismicity. This is an extensional step-over with two right-lateral strike-slip faults.

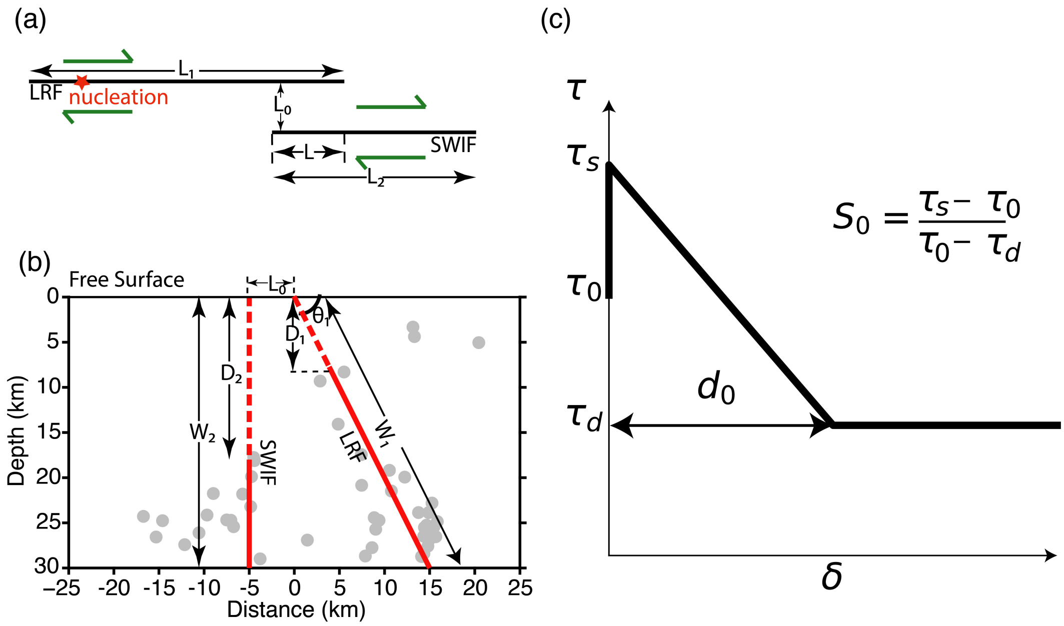

Figure 2. (a)-(b) Illustration of fault step-over geometry model in map view and cross-sectional view along the red line in Figure 1a. Earthquakes within 5 km to the transect line are plotted in (b). The dashed lines represent the buried fault segments. (c) A diagram showing the slip-weakening law and S_0. δ is the cumulative slip and τ is the shear stress on the fault.

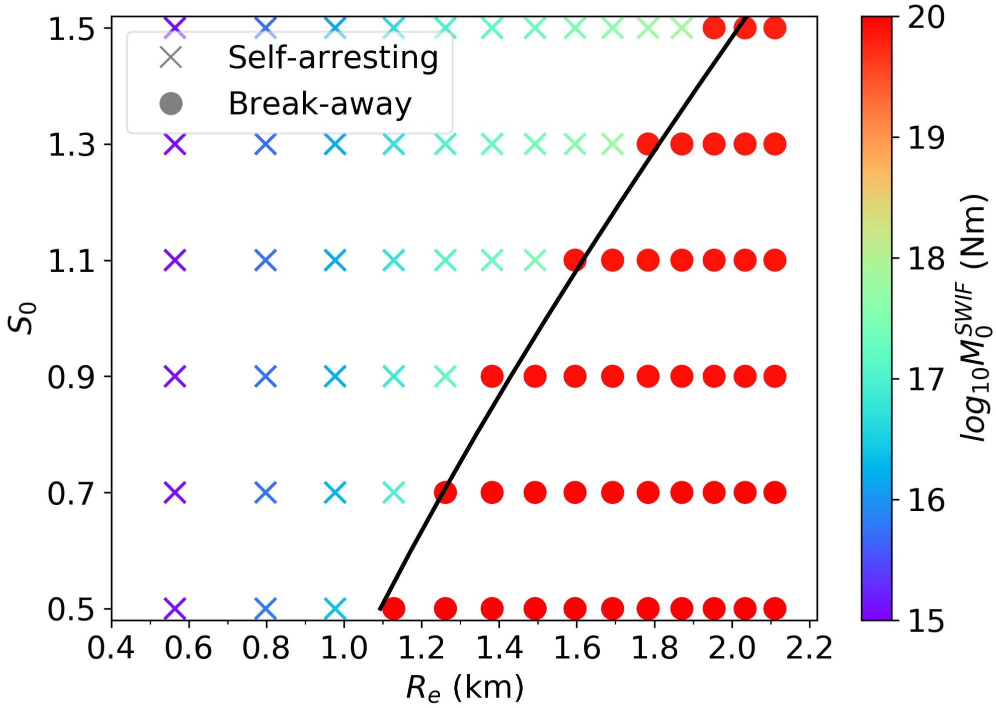

Figure 3. A phase diagram demonstrating the influence of the OSZ size R_e and initial stress level S_0 on rupture scenarios observed on a single fault modeled after the SWIF geometry. The black line marks the theoretical boundary estimated in Galis et al. (2015).

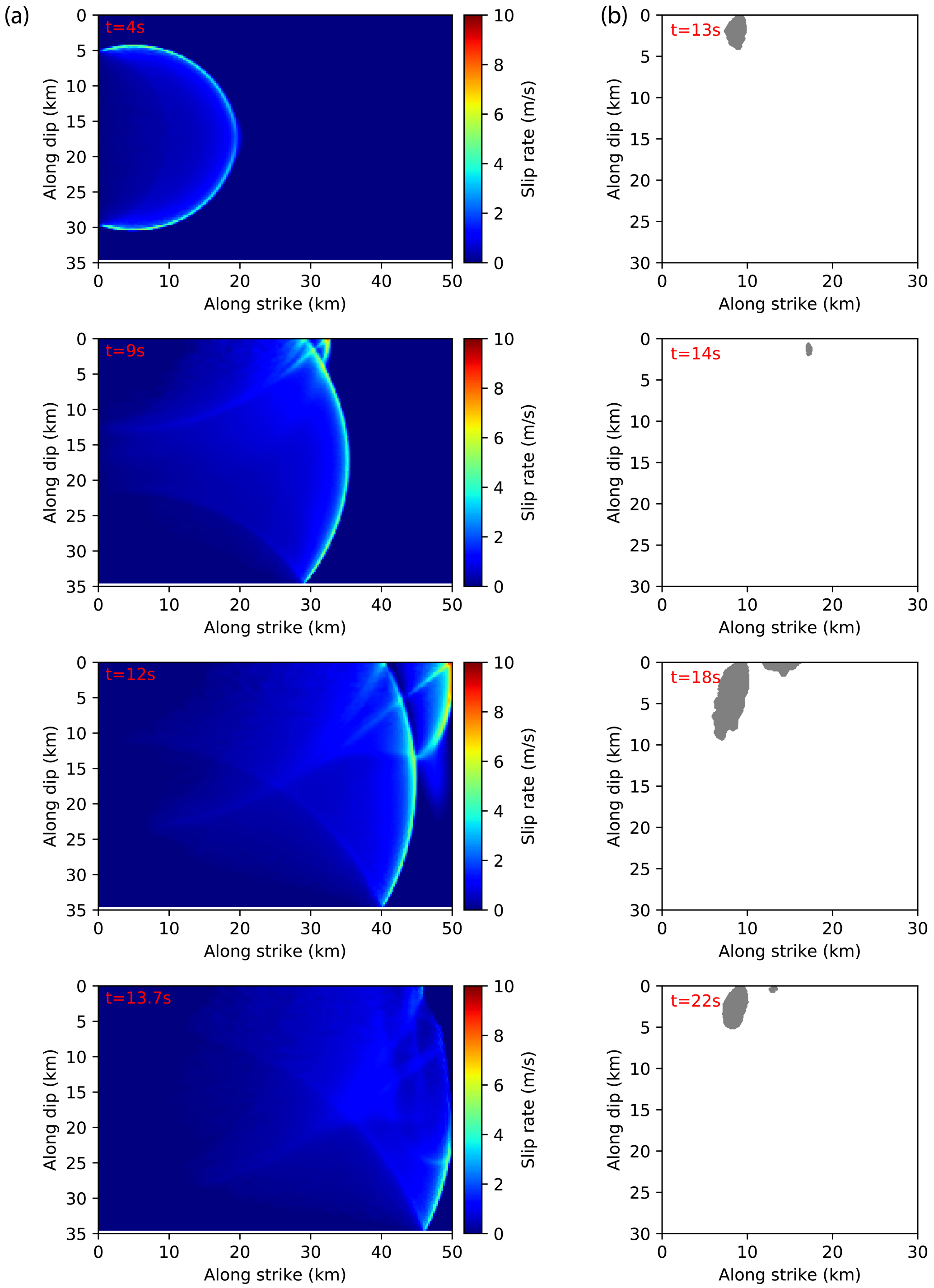

Figure 4. Simulation snapshots for $L_0 = 1$ km, $S_0 = 0.7$, $D_1 = 0$ km and $D_2 = 0$ km at different times for (a) the slip rates on the LRF and (b) the development of OSZ (shaded region) on the SWIF plane. t = 0 s indicates the initialization time of the LRF rupture.

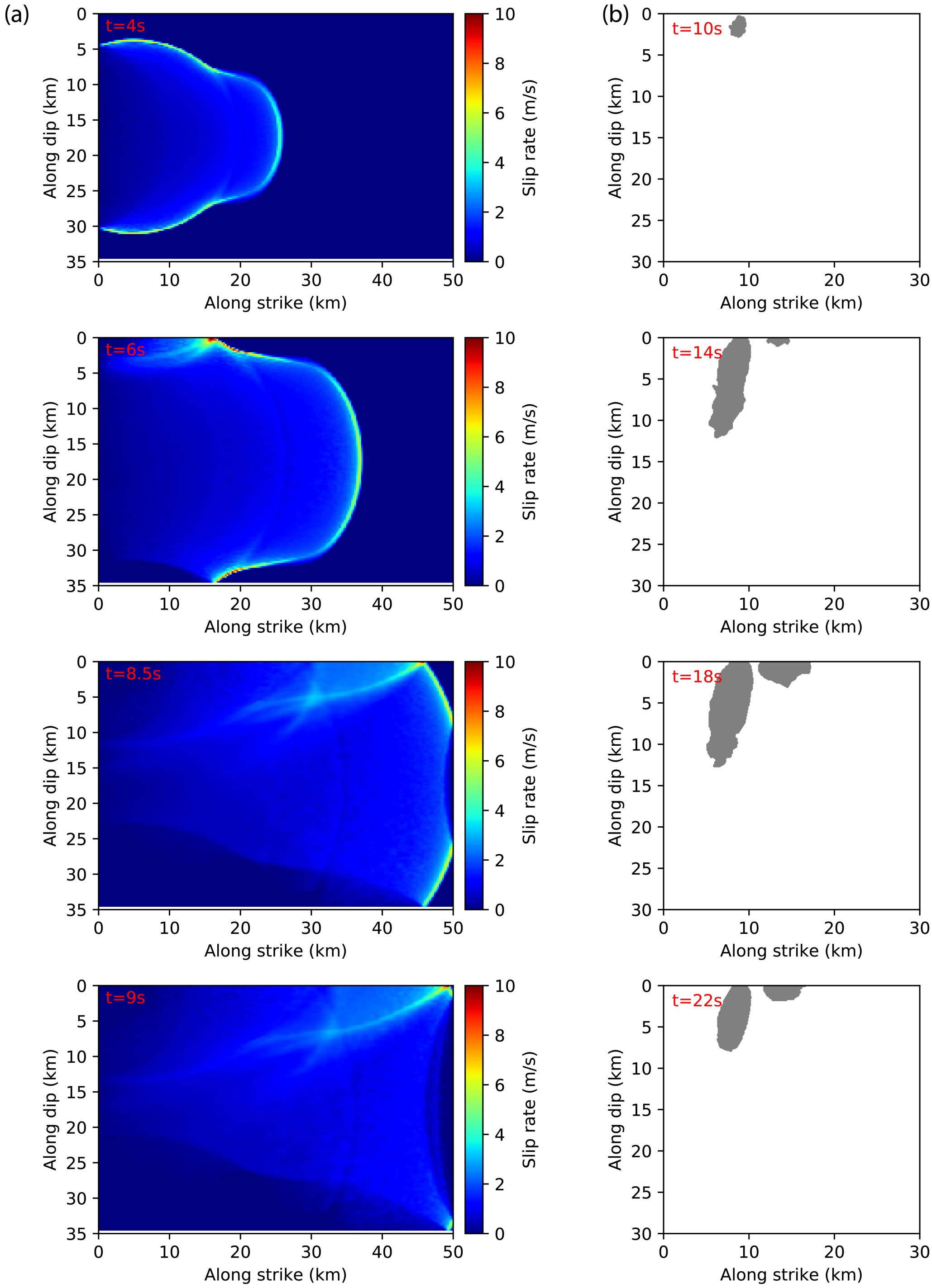

Figure 5. Similar to Figure 4, but for $L_0 = 1$ km, $S_0 = 0.5$, $D_1 = 0$ km and $D_2 = 0$ km.

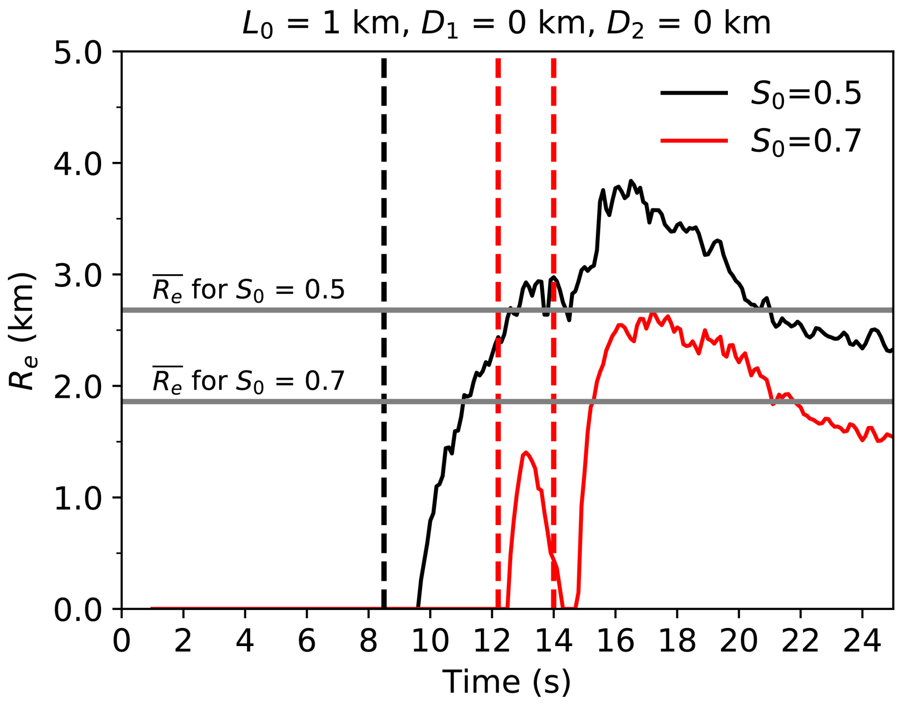

Figure 6. Curves showing the variation of R_e as a function of time for examples in Figures 4 and 5. The black and red vertical lines represent when the LRF rupture fronts meet the fault edge for simulations with S_0 = 0.5 and S_0 =0.7, respectively. Horizontal grey lines show $\overline{R_e}$ for two simulation cases.

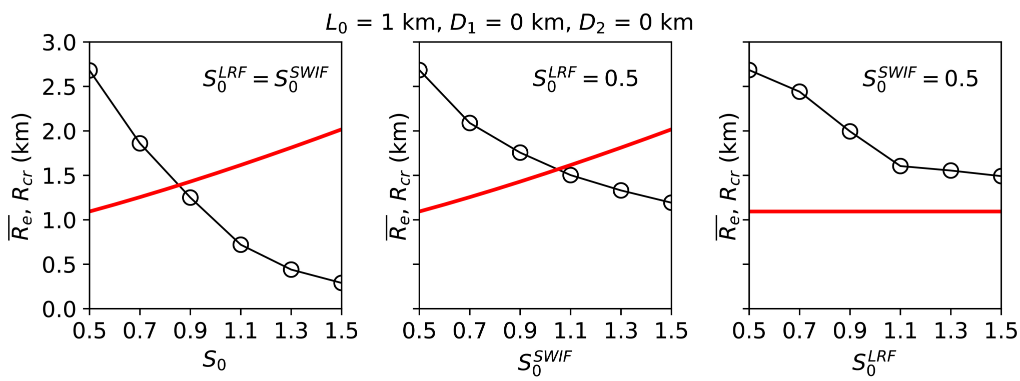

Figure 7. Curves showing $\overline{R_e}$ as a function of S_0 (when both faults are equally stressed), S_0^{SWIF} and S_0^{LRF}. The red lines represent R_{cr} estimated by Equation 7.

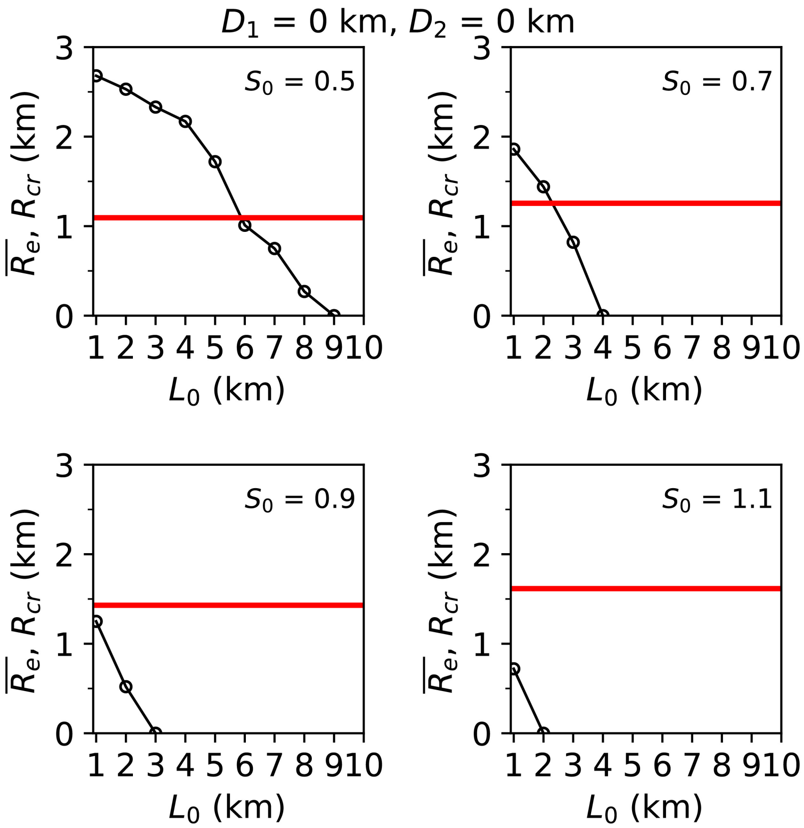

Figure 8. Curves showing $\overline{R_e}$ as a function of offset distance with different initial shear stress levels. The red lines represent R_{cr} at given S_0^{SWIF} estimated by Equation 7.

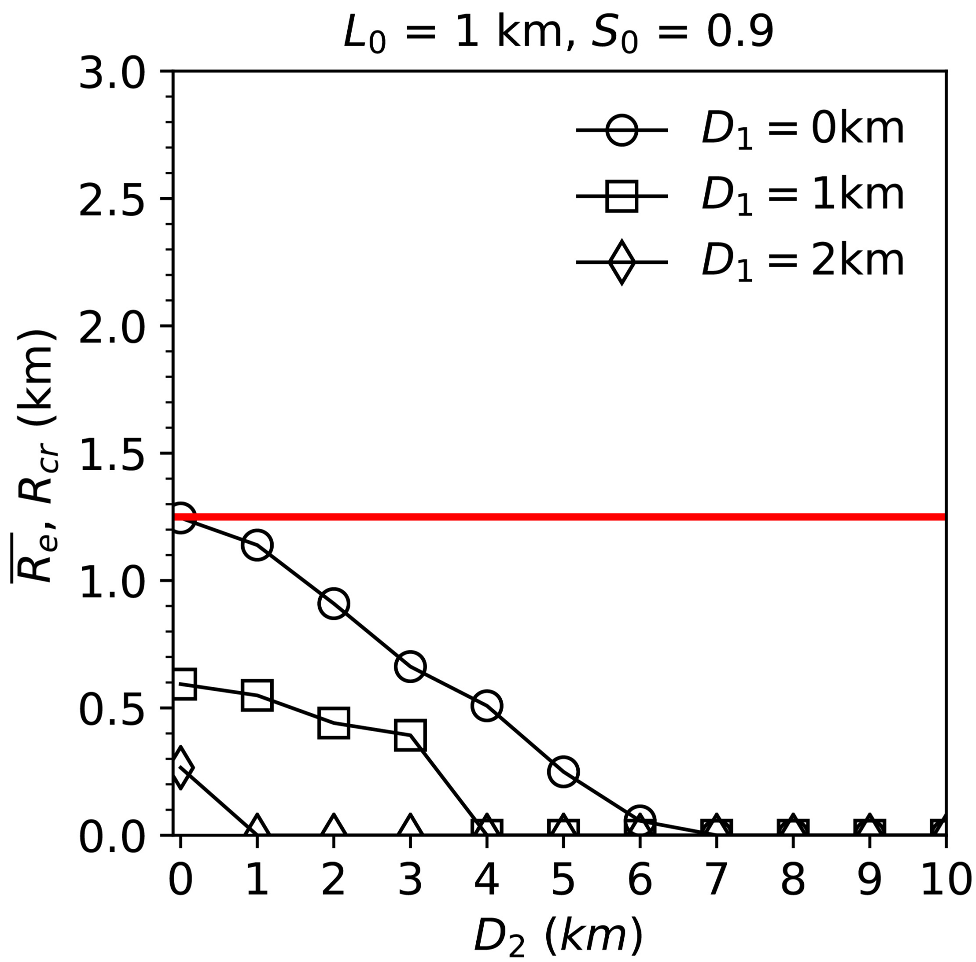

Figure 9. Curves showing $\overline{R_e}$ as a function of D_2 for different burial depths of the LRF. The red line shows R_{cr} for $S_0^{SWIF} = 0.9$.

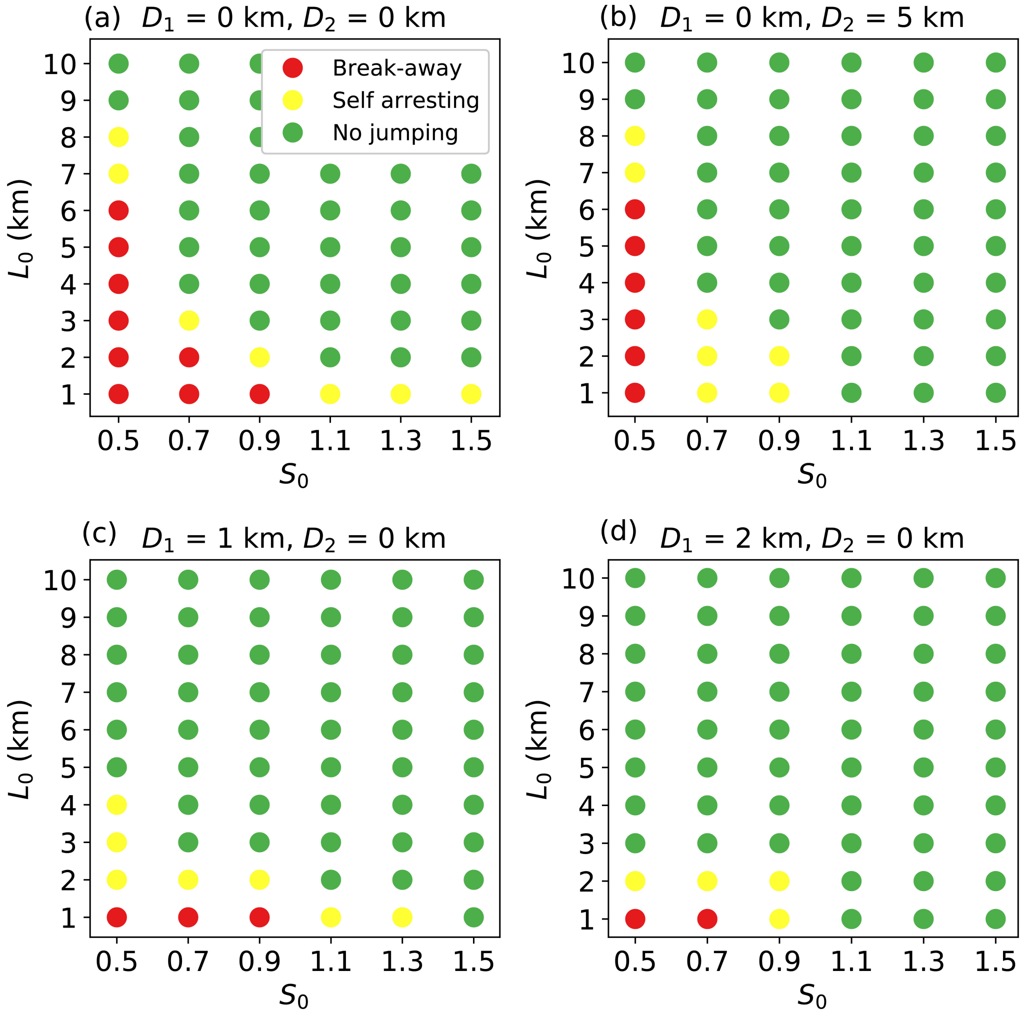

Figure 10. A phase diagram showing the effect of different parameters on rupture jumping scenario.

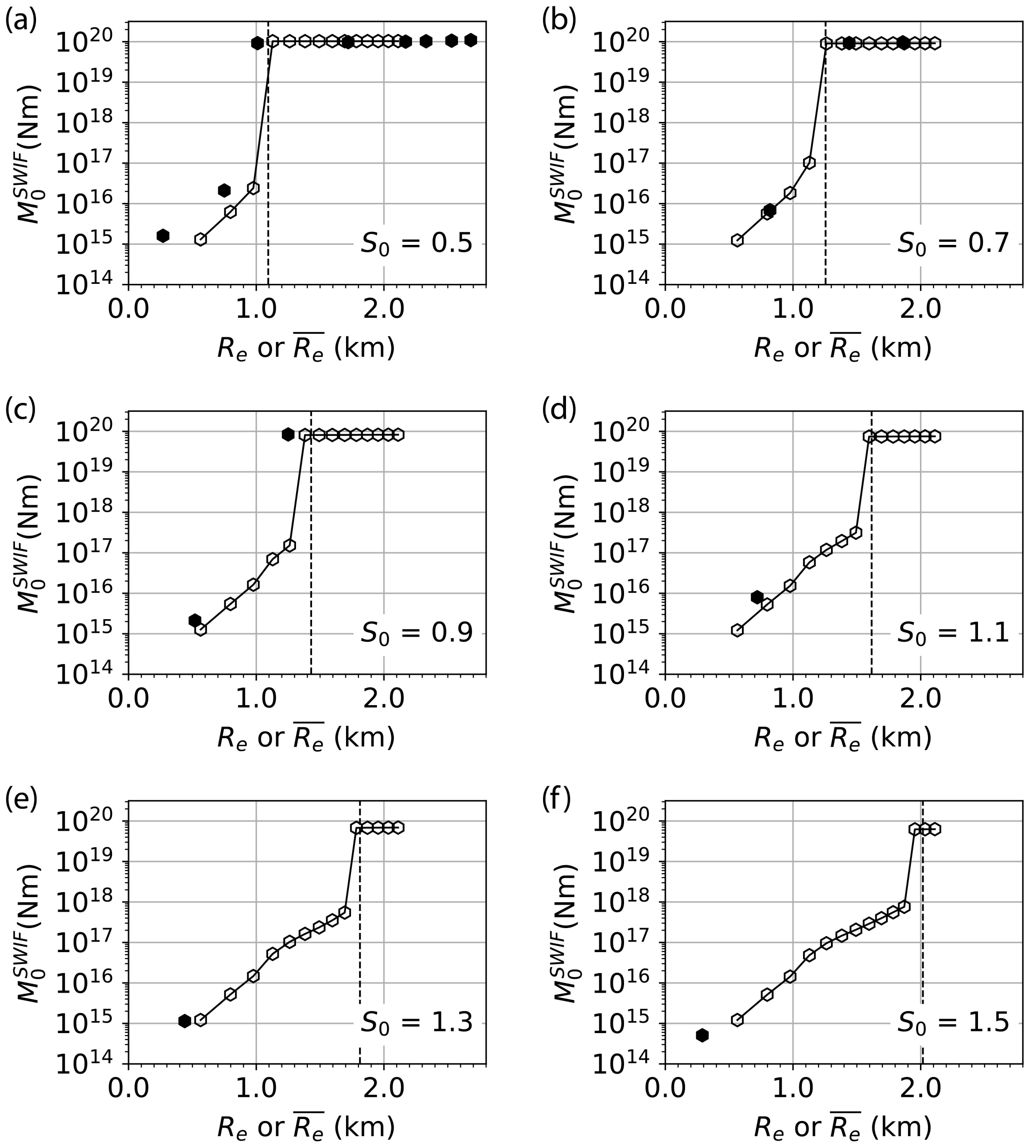

Figure 11. (a)-(f) Curves showing final SWIF seismic moment (M_0^{SWIF}) as a function of R_e (the nucleation zone radius in the initial comparative simulations discussed in Section 3) or $\overline{R_e}$ (the OSZ size observed in the first simulation set). Fixed model parameters are L_0 = 1 km, D_1 = 0 km, and D_2 = 0 km. The vertical black dashed line in each subplot represent R_{cr} estimated by Equation 7. Lines with open markers represent the (R_e, M_0^{SWIF}) data set and solid markers represent the ($\overline{R_e}$, M_0^{SWIF}).

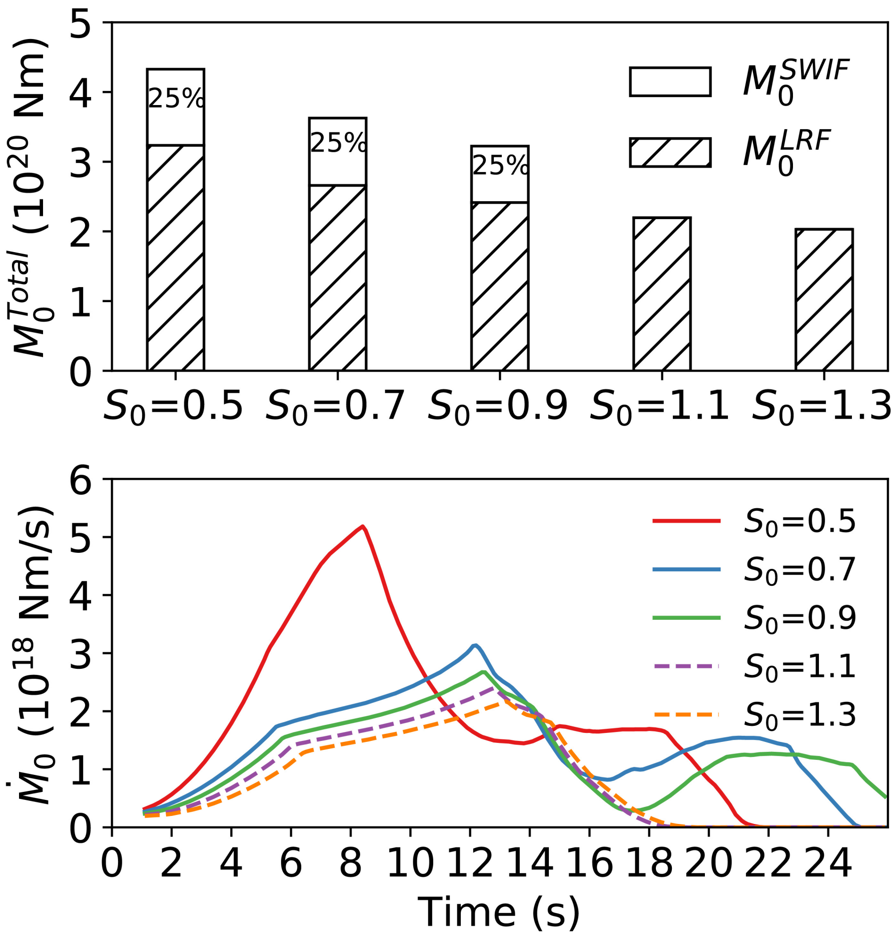

Figure 12. (a) Total seismic moment (M_0^{Total}) released and (b) moment release rate ($\dot{M}_0$) as a function of time at different initial stress levels, when $L_0 = 1$ km, $D_1 = 0$ km and $D_2 = 0$ km. The hatched and open area in (a) represent the contribution from the LRF and the SWIF, respectively. Solid lines in (b) denote the break-away ruptures on the SWIF, and dashed lines denote self-arresting ones.